This is a preprint, the final version is subject to change, of the American Mineralogist (MSA)
Cite as Authors (Year) Title. American Mineralogist, in press.
(DOI will not work until issue is live.) DOI: http://dx.doi.org/10.2138/am-2017-5984

Revised version 2

A nano-mineralogical study of samples from the Matoush Uranium ore deposit: Further evidence for the mobilization and agglomeration of uraninite nanoparticles

Michael Schindler[*1], Aaron J. Lussier[2], Jacob Bellrose[1], Sergei Rouvimov[2], Peter C. Burns[2, 3], and T. Kurt Kyser[4]

1. Department of Earth Sciences, Laurentian University, Sudbury, ON, P3E2C6, Canada
2. Department of Civil and Environmental Engineering and Earth Sciences, University of Notre Dame, Notre Dame, Indiana 46556, USA
3. Department of Chemistry and Biochemistry, University of Notre Dame, Notre Dame, Indiana 46556, USA
4. Department of Geological Sciences and Geological Engineering, Queen's University, Kingston, ON, K7L 3N6, Canada

Corresponding author: mschindler@laurentian.ca

Abstract

The occurrence of uraninite nanoparticles in the alteration zones of uranium ore deposits suggests potential mobilization of U(IV) under reducing conditions, which is important for understanding the mobility of uranium in contaminated sites and potential repositories for nuclear waste. This study investigates the occurrence of uraninite nanoparticles in the outer alteration zone of the Matoush uranium ore deposit, Quebec, Canada. Selected samples with finely disseminated uraninite from the outer alteration zone of the deposit are examined by X-ray fluorescence spectroscopy, scanning electron microscopy, and high-resolution transmission electron microscopy on specimens prepared using the focused ion beam milling technique. Uraninite nanoparticles occur as single particles, in clusters, and in larger aggregates in close association with the Cr-rich phases chromceladonite (Cr-rich mica), ideally $KMgCr^{3+}(Si_4O_{10})(OH)_2$, eskolaite , ideally $Cr^{3+}{}_2O_3$, bracewellite, $Cr^{3+}OOH$ and an amorphous Cr-rich oxide matrix as well as with fluorapatite and galena. Nanoparticles on the surface and in the outer rim of single uraninite crystals indicate the growth of larger uraninite crystals via crystallization through particle attachment and Oswald ripening. The flow texture of the uraninite nanoparticles in the amorphous Cr-rich oxide matrix, their aggregation on the surface of nanocrystals of bracewellite, the absence of products of a redox reaction involving U(VI) and Fe (II) and the occurrence of amorphous Fe-depleted alteration layers between uraninite and eskolaite, and uraninite and Cr-rich mica indicate that the uraninite nanoparticles have been mobilized under reducing conditions (leaching of Fe^{2+} from the alteration layer) at low T (amorphous character of the alteration layer) after the main mineralization event from the center of the mineralization to the outer parts of the Matoush dyke complex. These results indicate that fluids can mobilize U(IV) under reducing conditions in the form of uraninite nanoparticles albeit over limited distances. The potential mobilization of these nanoparticles may also explain the occurrence of proximal mineralized zones in U-ore deposits that lack common products resulting from the reduction of U(VI) by Fe(II) (*e.g.* hematite and other Fe^{3+}-phases).

INTRODUCTION

There is increasing interest in the occurrence of colloidal and crystalline nano-scale materials in the environment, as nanoparticles can transport metal(loid)s over significant distances and effectively sequester them in contaminated sites as well as ore deposits (Vilks et al. 1993; Kretzschmar and Schäfer 2005; Hochella et al. 2008; Weber et al. 2009). Colloids and crystalline nanoparticles are, in this regard, environmentally relevant for remediation strategies of U-contaminated sites and the design of nuclear waste repositories as they can transport and sequester radionuclides (Bargar et al. 2008; Dreissig et al. 2011; Schmidt et al. 2012, 2013; Bots et al. 2014; Suzuki et al. 2015). Uranium(IV) is typically thought to be immobile under reducing conditions, and that sequestration and containment of U and other radionuclides occurs under reducing conditions (Long and Ewing 2004). Uranium (IV)-bearing nanoparticles such as uraninite, coffinite and U-bearing silicates have been, however, identified in numerous studies (*e.g.*, Bargar et al. 2008; Dreissig et al. 2011, Wang et al. 2013; Fuchs et al. 2015, Riegler et al. 2015; Suzuki et al. 2015), suggesting that the mobility of U(IV) may be significantly enhanced by the presence of colloidal material under reducing conditions.

Uranium-ore deposits have been examined as natural analogues of nuclear waste repositories as their alteration halos provides valuable information on the mobilization and retardation of U and other radionuclides over millions of years (Pearcy et al. 1994; Fayek et al. 2003; Schindler et al. 2010). Recent nano- to microscale studies of finely disseminated uraninite in sandstone-hosted roll-front uranium deposits in northwest China (Min et al. 2005), organic matter at the Carbon Leader Reef, Witwatersrand Supergroup, South Africa (Fuchs et al. 2015) and in carbonaceous material in alteration halos around unconformity-related U deposits of the Kiggavik Camp, Nunavut, Canada (Riegler et al. 2016) indicated either the presence of uraninite nanoparticles or the occurrence of larger aggregates composed of uraninite nanoparticles. Fuchs et al. (2015) showed that uraninite nanoparticles have been either transported or formed under reducing conditions in hydrocarbon-bearing solutions and that larger aggregates of

78 uraninite formed through the attachment of individual particles. The latter observation suggests
79 that crystallization through particle attachment (CPA, De Yoreo 2015) may be a possible
80 mechanism for the formation of uraninite. The possibility of colloidal transport of U(IV) in U-ore
81 deposits and the subsequent growth of uraninite through *CPA* may address a long unanswered
82 question how uraninite ore bodies formed in alteration halos of redox-based U-ore deposits
83 where neither products of redox-reactions (e.g. hematite) or potential reductants of U(VI) (*e.g.*
84 Fe^{2+} minerals) have been observed in proximity to the ore (Hofmann 1999). For example,
85 mineralization of uraninite in roll front deposits may occur at a distance of 20 to 30 m from the
86 actual redox front and this has been interpreted to be the result of the common transport of
87 U(VI) with reducing species such as thiosulphates or microbes and the subsequent reduction of
88 U(VI) in areas of lower porosity (Hostetler and Garrels 1962; Granger and Warren 1969, 1974;
89 Reynolds and Goldhaber 1978, 1983; Goldhaber et al. 1978; Reynolds et al. 1982), rather than
90 being a product of the transportation, agglomeration and aggregation of uraninite nanoparticles.
91 The term *agglomeration* is used in this study when particles dispersed in solution attach to each
92 other forming irregular or regular shaped clusters or larger particles. The term *aggregation* is
93 used when nanoparticles or clusters of nanoparticles attach to already existing nano- to
94 micrometer size grains.
95 This study provides further evidence for the transport of uraninite nanoparticles under
96 reducing conditions in the alteration halo of a U-ore deposit, their agglomeration and
97 aggregation into larger uraninite grains through *CPA*. We propose that mobilization,
98 agglomeration and aggregation of uraninite nanoparticles in alteration halos of U-ore deposits
99 should be considered as an alternative model for the formation of some mineralization at greater
100 distances to redox fronts. Potential mobilization, agglomeration and aggregation of uraninite
101 nanoparticles evident at the Matoush deposit have application for the surroundings of a nuclear
102 waste repository.
103

The Matoush Uranium ore deposit

The Matoush uranium ore deposit lies within the Southwestern portion of the Otish Basin, located in Central Quebec (Fig. 1). A geological description of the latter basin can be found in Alexandre et al. (2015). The Matoush deposit is hosted in the Indicator Formation, a geological unit approximately 800 m thick that consists of conglomeratic sandstones and sub-arkose to arkosic sandstones (Alexandre et al. 2015). The ore deposit formed around the bimodal Matoush dyke (Fig. 1), which averages 1.6 m in thickness and intruded into the Indicator Formation along the Matoush Fracture (Gatzweiler 1987; Alexandre et al. 2015). The Matoush dyke is predominantly mafic but is cross-cut by a smaller felsic pegmatite dyke (Fig. 1). The mafic dyke contains mostly plagioclase, magnetite and biotite with minor pyrite, chalcopyrite, and galena. In altered porous segments of the dyke, these minerals have been partly replaced by biotite, chlorite, hematite and minor calcite (Gatzweiler 1987). The felsic pegmatite dyke consists of grains of feldspar, quartz, and tourmaline, each averaging 1 mm in thickness. A 50-m-wide alteration halo is observed to be nearly symmetric around the Matoush dyke and consists of an inner tourmaline alteration zone, outer Mg–chlorite and Cr–V mica zone, and an outermost halo of limonite and hematite (Fig. 1, Gatzweiler 1987). Uranium mineralization is distributed on both sides of the Matoush Fracture, and ranges from1 to 20 m in thickness. It always occurs in the core with altered segments of the dyke but never with the unaltered counterparts. The U-mineralization consists of massive and semi-massive uraninite in both the core and inner alteration zones, and of disseminated uraninite and uranophane within the Cr-bearing minerals dravite, chromphyllite and eskolaite in the outer alteration zone (Alexandre et al. 2015).

Uranium was most likely mobilized from refractory phases such as zircon, monazite, and fluorapatite contained in the Indicator Formation sandstones by oxidizing basinal brines. Additional sources for U were most likely U-bearing minerals in the pegmatite portion of the Matoush dyke. Alexandre et al. (2015) argued that the massive and semi-massive pods and

lenses of uraninite in the core and inner alteration zone formed through the oxidation of Fe^{2+} and sulfide minerals in the Matoush dyke such as magnetite, biotite, plagioclase, and minor pyrite. The authors further suggested that the more disseminated uraninite mineralization in the outer alteration zone formed through the oxidation of Fe^{2+} rather than Cr^{3+} in Cr-bearing tourmalines and micas, as the redox potentials for the half-cell reactions $U^{4+} + 2H_2O \rightarrow (U^{6}O_2)^{2+} + 4H^{+} + 2e^{-}$ (E_0 = +0.27 eV) and $2Cr^{3+}$ (aq) + $7H_2O \rightarrow (Cr_2O_7)^{2-}$(aq) + $14H^{+}$ (aq) + 6e- (E_0 = +1.33 eV) indicate thermodynamically unfavourable conditions for the reduction of $(U^{6+}O_2)^{2+}$ by Cr^{3+}.

Sample location and paragenetic sequence

The absence of Fe^{3+}-oxide minerals in the disseminated uraninite mineralization (i.e. the common end-products of the oxidation of Fe^{2+}-minerals and reduction of U^{6+}-aqueous species) prompted us to further investigate the texture and chemical composition of uraninite and associated minerals at the nano-scale. A representative sample from the U-mineralized portion of drill core MT-34A drill was taken at approximately 300 m vertical depth. The mineralized portion of this drill core is in close proximity (~20m) to the mineralized area of the drill core MT0610-DDH10 for which a detailed paragenetic sequence has been described by Beyer and Kyser (2015). In the latter core samples, fluorapatite is the oldest paragenetic phase followed by various forms of a Fe-bearing eskolaite, which formed during the intrusion of Cr-rich magmatic fluids after the dyke emplacement (Alexandre et al. 2015; Beyer and Kyser 2015). Eskolaite has been partially replaced by tourmaline in these samples and both minerals have been subsequently altered to chromphyllite. Uraninite mineralization (~1008 ± 80 Ma, Pb-Pb age) follows these Cr-rich metasomatisms, which in turn is followed by minor pyrite, clausthalite and quartz and subsequent fluid events that variably altered the uraninite by adding Ca, Si and Fe and removing radiogenic Pb (Beyer and Kyser 2015).

EXPERIMENTAL

A sample from the U-mineralized portion of drill core MT-34A with finely disseminated uraninite was prepared for optical microscopy, micro X-ray fluorescence (μ-XRF), scanning electron microscopy (SEM), and X-ray powder diffraction (XRD). Two Focused Ion Beam milled sections (20 x 8 μm) were extracted from a thin section and subsequently examined with transmission electron microscopy (TEM). Minerals were identified using a combination of the analytical methods listed above.

Optical microscopy, scanning electron microscopy, X-ray powder diffraction and X-ray fluorescence spectroscopy

Mineralogical, morphological, and textural relationships of both thin sections were examined with a petrographic optical microscope and a JEOL JSM-6400 SEM operating at 20 kV with a probe current of 1 nA. X-ray powder diffraction patterns were recorded with a Panalytical X'pert Pro Powder diffractometer using Co Kα radiation (λ = 1.79 Å) at 40 kV and 30 mA. Diffraction patterns were collected over a 2θ range of 5-75° with a step size of 0.02° and counting time of 2 s step^{-1}. Chemical maps were recorded using an EDAX Orbis micro- X-ray fluorescence (XRF) spectrometer operating at 50 kV, 900 μA and with a dwell time of 0.1 s.

Focused ion beam (FIB) technology and transmission electron microscopy (TEM)

A FEI Helios Dual Beam 600 NanoLab instrument was used to prepare electron-transparent sections. Prior to their introduction to the FIB vacuum chamber, the samples were sputter-coated with iridium to prevent charging from the ion/electron beams. Sections 1 and 2 were extracted at approximately perpendicular orientations to contacts between uraninite / Cr-rich mica / fluorapatite, and eskoaite / Cr-rich mica / uraninite, respectively. Both resulting sections had dimensions of circa 20 μm length by 8 μm height. After preliminary excavation, each section was temporarily fastened, using sputtered platinum, to an OmniProbe 200

nanomanipulator for removal from the bulk sample and subsequent milling to electron transparency; a Ga^{2+} ion beam was used for both excavation and milling. Each section was mounted onto a copper holder. Further details on the extraction of FIB sections from geological material can be found in review articles by *e.g*. Wirth (2009) and Lee (2010).

The sections were examined using a FEI Titan 800-300 transmission electron microscope (TEM) at the University of Notre Dame Integrated Imaging Facility. Measurements were taken using an acceleration voltage of 200 kV and a beam current of 107 µA. Selected area electron diffraction (SAED) patterns were obtained using a Gatan 4x4k bottom-mount charge coupled device camera. Electron dispersive spectroscopy (EDS) point analyses were collected in scanning transmission electron microscope mode (STEM) with an Oxford INCA 30 mm^2 LN_2 detector. The sections were also examined using a JEOL 2100 TEM (a field thermionic emission analytical electron microscope) at Virginia Polytechnic Institute. Measurements were taken using an accelerated voltage of 200 kV and a beam current of 107 µA. EDS point analyses and maps were acquired in STEM mode using a JEOL BF detector. SAED patterns were acquired using a Gatan Orius SC200D detector.

RESULTS

Petrographic examinations, *µ*-XRF chemical distributions map (Fig. 2a-e) and powder XRD (supplementary data) of the selected sample from the U-mineralized portion of drill core MT-34A indicate the occurrence of the major phases eskolaite (blue in Fig. 2b, c), chromium dravite, $(Na(Mg, Fe^{2+})_3(Cr, Al)_6(Si_6O_{18}(BO_3)_3(OH)_3(OH)$ with Mg > Fe^{2+} and Cr^{3+} > Al) (dark green in Fig. 2b, c), uraninite (green in Fig. 2d, e and white in Fig. 2g-i), fluorapatite (violet in Fig. 2e, green in Fig. 2g) and quartz (yellow in Fig. 2b and d). Traces of chromceladonite (Cr-rich mica) $(K, Ca)(Mg, Fe)_1(Cr, Al)_{,0.67}(AlSi_3O_{10})(OH)_2$ with K > Ca, Mg > Fe and Cr > Al (a phase similar in composition to chromphyllite but with Mg > Cr) , bracewellite, (CrOOH) and galena, (PbS) were only detected with SEM and TEM.

Eskolaite occurs as massive to botryoidal (Fig. 2 b-c), whereas chromium dravite displays euhedral elongated prismatic crystals 2.5 mm in length by 0.1 mm width, with less abundant subhedral to euhedral cross-sections (Fig. 2 b-c, green in Fig. 2e). Fluorapatite appears as colourless anhedral to euhedral crystals with blocky to hexagonal habit, 0.2 mm and 1 mm in size respectively (Fig. 2e). Alteration of fluorapatite is commonly associated with the occurrences of uraninite and altered chromium dravite. Uraninite occurs finely disseminated as intercrystalline fillings in either eskolaite or chromium dravite, or follows fluorapatite and eskolaite boundaries and fractures (Fig. 2d-e, h). Chromium-rich mica is closely associated with uraninite mineralization throughout the sample, often surrounding its boundaries at the micrometer scale (Fig. 2g-i). Uraninite grains can contain significant amounts of impurities with maximum concentrations for Si with 10 at%, Al and Pb with 5 at% and Ca and Fe with 3 at%.

Focused ion beam sections: locations and mineralogy

An inherent limitation of the FIB/TEM approach employed here is that the area to be investigated is physically limited and thus represents only a very small fraction of the geological area of interest. Hence, locations for their extraction must be carefully chosen such that the section contains multiple interfaces or characteristic morphological features. In the current work, locations for the FIB section extractions were selected on the basis of the number of interfaces between uraninite and adjacent minerals on the micrometer scale. Section 1 includes common interfaces between uraninite and the Cr-rich mica and uraninite and fluorapatite (Fig. 2g) and Section 2 contains interfaces between uraninite and Cr-rich mica and Cr-rich mica and eskolaite (Fig. 2h-i).

In the extracted FIB sections, uraninite, fluorapatite, Cr-rich mica and an amorphous Cr-rich matrix are the major phases with minor galena (Section 1), coffinite and $USiO_4$ (Section 2) and traces of bracewellite ($Cr^{3+}OOH$) (section 2). SAED pattern with *d*-spacings and EDS chemical distribution maps for these identified phases can be found in the supplementary data.

Section 1 contains interfaces between uraninite and fluorapatite, Cr-rich mica and galena. The latter phase occurs as a single crystal recognizable as the altered (111) face of a cuboctahedron (Fig. 3a). Section 2 contains interfaces between uraninite, Cr-rich mica and an amorphous Cr-rich oxide matrix (Fig. 3b and c) with predominantly Cr (>30 at%), minor Ca, Al, Si, Mg and U (<5 at%) and traces of Fe (<1 at%). In comparison, eskolaite adjacent to uraninite at the micrometer scale (Fig. 2h and i) contains minor Fe (<5 wt%), traces of Ca, Al, Si and Mg (<1 at%) and no detectable amounts of U (on the basis of EDS/SEM). Eskolaite itself could not be identified in Section 2 as the eskolaite-dominated part of the section was mounted directly to the Cu sample-holder and thus was not accessible for TEM examinations (Fig. 3b).

Features along the uraninite-fluorapatite and uraninite-galena interfaces in Section 1

Nanoparticles of uraninite are finely disseminated along the fluorapatite surface as well as along fillings between fluorapatite and galena (Fig. 4a). The interfaces between uraninite and fluorapatite, and between uraninite and galena, are both characterized by the absence of alteration layers between the nano-size domains of uraninite and the surfaces of fluorapatite (or galena). Lattice fringes of uraninite are in direct contact with those of fluorapatite and galena (Fig. 4b-d). The nano-size domains of uraninite are intergrown, display irregular outlines and have different orientations recognizable on the changing orientation of the dominant (111) lattice fringes with d = 3.15 Å (Fig. 4b-d). In contrast to uraninite, the near-surface structure of fluorapatite is characterized by lattice fringes of uniform orientation with d = 5.25 (101) (Fig. 4b). Lattice fringes in the near-surface structure of galena are difficult to recognize due to the thickness of the crystal, but fringes parallel to (220) and (200) are visible at two locations (Fig. 4c and d). Larger particles of uraninite are composed of mainly single crystals recognizable from their SAED pattern with sharp diffraction spots (i.e. they are not aggregates of nanoparticles) whereas areas composed of nanoparticles of different orientations produce SAED patterns with diffraction rings (Fig. 4a).

Features along the uraninite-Cr-rich mica interface in Section 1

The structure and composition of the interface between uraninite and Cr-rich mica were investigated with a sequence of SAED patterns and with chemical distributions maps for U, Si, Al, Cr and Fe (Fig. 5). A circa 0.5 μm thick alteration layer occurs between uraninite and Cr-rich mica (Fig. 5a, b). This layer is either amorphous or poorly crystalline (no diffraction spots are observed in the corresponding SAED pattern, Fig. 5c) and is highly depleted in both Fe and Mg, slightly depleted in Cr, and enriched in Si, Al and U relative to the Cr-rich mica. The SAED pattern indicates that the core of the uraninite is predominantly composed of a single crystal (sharp diffraction spots and no rings, Fig. 5c) whereas areas in proximity to the uraninite surface consist of a higher number of nanocrystals with different orientations (diffraction spots and rings; Fig. 5c). The occurrence of uraninite nanocrystals of different orientations is also observed at the surface of the uraninite single crystal in proximity to the galena crystal where three nanocrystals of uraninite are visible proximal to its surface (Fig. 5d).

Features along the uraninite-Cr-rich oxide matrix interface in Section 2

Figures 6 and 7 show detailed STEM-EDS and TEM data acquired on two regions of Section 2 (as indicated in Figure 3c). Uraninite occurs in an amorphous Cr-rich oxide matrix in the form of individual or aggregated nanoparticles. The interface between aggregated (Fig. 6a, b) and individual (Fig. 6c) nanoparticles and the Cr-rich oxide matrix is characterized by an amorphous alteration layer depleted in Fe and Mg and enriched in Si and Al (Fig. 6a- c) whereas Cr occurs in similar proportions in the alteration layer and in the Cr-rich oxide matrix (see also Fig. 7e). In proximity to the uraninite nanoparticles, assemblages of single crystals of bracewellite occur. These crystals can be up to 50 nm long and display well developed lattice fringes with d = 4.9 Å (020) (Fig. 6d-f).

Texture and mineralogy of individual and aggregated nanoparticles in Section 2

Most of the nanoparticles in Section 2 are composed of uraninite. Individual nanoparticles are slightly ellipsoidal with axial lengths ranging from 30 to 100 nm (Figs. 6c, 7b). These nanoparticles are thus ~10 to 20 times larger than biogenic uraninite nanoparticles (Bargar et al. 2008) and the aggregated nano-domains observed on the surfaces of galena and fluorapatite (Fig. 4b-d). Nanoparticles of coffinite are less common (Fig. 7c) and are poorly crystalline displaying SAED patterns with diffuse peaks or rings (supplementary data).

The arrangement of uraninite nanoparticles along the interface to the Cr-rich mica in Section 2 resembles a flow texture of nanoparticles in a porous medium (Fig. 7a). Uraninite nanoparticles located in, or adjacent to, this flow path occur as individual nanoparticles (especially among the Cr-rich mica lathes, Fig. 7a), as clusters of two to five agglomerated nanoparticles (Fig. 7b) or as highly condensed aggregates around fibrous inclusions (indicated with arrows in Fig. 7a, d-e). Chemical distribution maps and SAED patterns indicate that these inclusions are composed of bracewellite (Figs. 7d-e, supplementary data).

DISCUSSION

The distribution of disseminated uraninite from the outer mineralized zone of the Matoush dyke coincides with grain boundaries between the earlier formed fluorapatite, Cr-dravite, eskolaite and Cr-rich mica. Alteration features and products associated with the finely disseminated mineralization include corroded surfaces of fluorapatite and galena, an amorphous Cr-rich oxide matrix, Fe-Mg-depleted and Si-Al-enriched alteration layers, coffinite nanoparticles and bracewellite needles in the Cr-rich matrix in Section 2. The Cr-rich oxide matrix in Section 2 (Figs. 3c and 6a-e) and the Si-Al-enriched alteration layer located between uraninite and Cr-rich mica in Section 1 (Fig. 5a and b) are most likely products of the alteration of eskolaite and Cr-rich mica, respectively. The additional presence of a Fe-depleted nano-scale alteration layer between uraninite and the Cr-rich oxide matrix in Section 2 indicates the

311 involvement of at least two distinct fluids (Fig. 8); an earlier fluid that altered eskolaite to a Cr-
312 rich oxide matrix and that promoted the recrystallization of bracewellite needles within this
313 matrix and a later uraninite nanoparticle-bearing fluid that altered the Cr-rich oxide matrix
314 through the additional removal of Fe and addition of Si, and deposited the uraninite
315 nanoparticles in the pore spaces produced by the earlier alteration fluid (Fig. 8).
316
317 **Formation of the Fe-depleted and Si-Al enriched alteration layers**
318 The formation of a Fe-depleted and Al-Si enriched alteration layer on the surface of Cr-rich
319 mica (Section 1) and eskolaite (Section 2) indicate that the fluids had a near neutral pH value as
320 the alteration did not result in the removal of amphoteric Al and Cr^{3+} (Fig. 8) The fluids must also
321 have been reducing as their interaction with Cr-rich mica and eskolaite resulted in the removal
322 of Fe which is only mobile under near-neutral pH-conditions in its divalent state. This conclusion
323 is supported by the uraninite nanoparticles being stable under reducing conditions as they are
324 more susceptible to oxidation than their micrometer-size counterparts (Suzuki et al. 2002).
325 Alteration under reduced conditions is also in agreement with the presence of the trivalent Cr-
326 hydroxide mineral bracewellite and the preservation of most parts of the galena crystal. The
327 amorphous character of the Cr-rich oxide matrix and the interface between uraninite and Cr-rich
328 mica indicate alteration at low T as (a) the occurrence of bracewellite needles in the Cr-rich
329 matrix indicates only partial recrystallization of the Cr-rich matrix (Fig. 7d-f) and as (b) high-T,
330 processes would have most likely resulted in the complete recrystallization of these alteration
331 phases.
332
333 **The presence of uraninite nanoparticles: products of transportation or an *in situ***
334 **reduction process?**
335 Fuchs et al. (2015) could not completely answer the question whether the observed
336 uraninite nanoparticles in bitumen at the Carbon Leader Reef, Witwatersrand Supergroup

337 formed *in situ* through the reduction of U^{6+} by hydrocarbon-bearing fluids or whether they were
338 transported by these fluids and subsequently deposited. Similarly, the uraninite nanoparticles
339 observed in Sections 1 and 2 could have been either transported and deposited by reducing
340 fluids (*i.e.* a physical process) or formed through the *in situ* reduction of U^{6+} by reducing ions in
341 the fluids (*i.e*. a chemical process). In the latter case, possible reductants of U^{6+} could have
342 been Fe^{2+} and reduced S-bearing species, both released through the alteration of mafic
343 minerals and sulfides in the Matoush dyke. Hydrocarbon-bearing fluids and microbial activity
344 cannot be completely ruled out but evidence for them is lacking in previous studies of the basin
345 (e.g. Gatzweiler 1987, Alexandre et al. 2015). Reduced sulfur-bearing species may have been
346 present in the fluids but most likely at low concentrations as sulfides are only a minor
347 component in the mafic part of the Matoush dyke (Alexandre et al. 2015). Dissolved Fe^{2+} may
348 have been also present in small concentrations as only 3 at% Fe occurs in uraninite and as
349 Fe^{3+}-minerals, products of the oxidation of Fe^{2+} and reduction of U^{6+}, are not observed in
350 proximity to the disseminated ore. Furthermore, it seems unlikely that a Fe^{2+}-rich solution with
351 Fe and U would have altered Cr-rich mica and eskolaite to secondary phases depleted in Fe.
352 Thus it is unlikely that large amounts of reducing S- and Fe-bearing species could have reduced
353 U^{6+} species *in situ* in the outer mineralized zone of the Matoush dyke.

354 Hence, we propose here that the uraninite nanoparticles formed either after or during the
355 main mineralization event through the reduction of U^{6+}-bearing brines by Fe^{2+}-mafic minerals
356 within the Matoush dyke and were transported by reducing fluids at a later stage to the outer
357 alteration zones of the ore deposit (Fig. 8) in accordance with the observed flow texture of the
358 uraninite nanoparticles within the Cr-rich matrix (Fig. 7a).

359 Conditions that favour the formation of (abiotic) nanoparticles versus larger single crystals
360 are a high degree of supersaturation or a high number of surface sites that promote the
361 simultaneous homogenous and heterogeneous nucleation of a large number of crystals. If these
362 conditions indeed occurred in the center of the Matoush dyke, fluids could have easily

transported the highly mobile uraninite nanoparticles from the inner to the outer parts of the mineralized zone at a later stage.

The depletion of Fe^{2+} in alteration layers around the Cr-rich mica can be simply explained by the dissolution of the latter silicate, the subsequent reprecipitation of the amorphous Cr-Al-silicate and the removal of the mobile Fe^{2+}. This process cannot, however, explain the removal of Fe^{3+} present in eskolaite and the Cr-rich oxide matrix. The elimination of this cation would have required its reduction to Fe^{2+}, which may have been facilitated by U^{4+} -bearing aqueous species or by the dissolution of uraninite nanoparticles and the subsequent removal of Fe^{2+}- and uranyl-aqueous species (Fig. 8). The presence of U^{4+}-bearing aqueous species or the dissolution of uraninite nanoparticles may also explain higher U-concentrations in the Cr-rich oxide matrix (1- 5 at% U) and the alteration layer between uraninite and the Cr-rich mica (1-2 at% U) relative to eskolaite and Cr-rich mica, respectively.

Agglomeration, aggregation and retardation of nanoparticles

In the two FIB sections examined here, uraninite occurs either in the form of individual nanoparticles, aggregations of nanoparticles, strongly intergrown nano-domains and as larger single crystals (Figs. 4-7). These distinct features indicate different stages of agglomeration and aggregation of nanoparticles and suggest the formation of single crystals through crystallization by particle attachment (*CPA*).

Agglomeration of nanoparticles in fluids occurs when physical processes bring particle surfaces in contact with each other and short-range thermodynamic interactions allow for particle attachment to occur. For particles <100 nm in size, Brownian diffusion controls the long-range forces between individual nanoparticles, causing collisions between particles (Hotze et al. 2010). When contact occurs, it can result in either attachment or repulsion. Short-range thermodynamic interactions that control the collision of nanoparticles can be understood in the context of the Derjaguin-Landau-Verwey-Overbeak (DLVO) theory which describes the relative

effects of both repulsive and attractive forces. According to this theory, the sum of attractive and repulsive forces determines attachment (Derjaguin and Landau 1941; Verwey et al., 1948) whereby van der Waals (vdW) forces and electrostatic double layer (EDL) forces are the dominant attractive and repulsive forces, respectively.

The settling and agglomeration of nanoparticles depends on chemical and physical properties of fluid and nanoparticles such as the density of nanoparticles, the geometry and openness of the flow path and whether the flow is laminar or turbulent; *i.e.* the higher the particle density and Dean number and the lower the permeability and Reynolds number, the greater the degrees of settling and agglomeration (e.g. Choi et al. 2013; Liyanage et al. 2016). Attractive and repulsive forces during the collision of nanoparticles are also controlled by the surface charge, particle size and shape of the nanoparticles, types of ionic species in solution, alteration layers and adsorbed species on the surface. The surface charge itself is controlled by the point of zero charge of the nanoparticle, which in turn is affected by the chemical composition, particle size, adsorbed species and alteration features on the surface (see Hotze et al. 2010 for details).

Uraninite has a point of zero charge of pH_{pzc} = 5.5 (Olsson et al. 2002; Singer et al. 2009); however, for either nanoparticles of uraninite or uraninite with a surface oxidation layer containing U^{6+} or adsorbed cationic and anionic aqueous species, the pH_{pzc} is typically observed to be lesser or greater than this value (Hotze et al. 2010). Variable concentrations of aqueous species in the fluids and on the surface of the nanoparticles also affect agglomeration and thus mobilization of the particles, as smaller and larger concentrations of ions in fluids and on surfaces result in an increase or decrease in the repulsive forces between the particles, respectively (Hotze et al. 2010).

Another important factor to consider is the presence of clay and metal-oxide colloids in the fluids, as these can promote retention and aggregation of nanoparticles due to differences between the surface charges of the clay/oxide and the nanoparticles (Schmidt et al. 2012, 2013;

Cai et al. 2014). For example, the clustering of uraninite nanoparticles around needles of bracewellite (Fig. 7a and d-e) suggests the aggregation of the former particles on the latter needles. This so-called heteroaggregation process was most likely dominant during mineralization in the area examined in Section 2, as most of the larger uraninite aggregates are clustered around the earlier-formed bracewellite needles (Fig. 7a, d-e, Fig. 8).

To conclude, the geometry and permeability of the flow path along the Cr-mica-eskolaite grain boundary, the presence of bracewellite needles and aqueous species in the fluids and adsorbed to the nanoparticles were most likely factors that controlled the agglomeration, aggregation and thus the retention of the nanoparticles observed in the Sections 1 and 2. Individual nanoparticles occurring among the Cr-rich mica lathes were presumably adsorbed by the latter substrate, but the absence of larger aggregates in this area of Section 2 suggests that the adsorption process did not promote the aggregation of a large number of nanoparticles.

Crystallization *via* particle attachment

An increasing amount of evidence indicates that crystallization through particle attachment (CPA) is a significant mechanism by which crystals nucleate and grow (Colfen and Antonietti 2008; De Yoreo et al. 2015). In contrast to the conventional model of crystal growth, *i.e.*, one in which individual ligands are added sequentially to a growing crystal face, *CPA* results from the attachment of already-formed particles in the proximal, nascent fluid to the growing crystal face. Where the particles are amorphous, their aggregation proceeds by an amorphous-to-crystalline pathway that results in a final single crystal (a characteristic feature in many biogenic systems). In the case of crystalline nanoparticles, aggregates attach to a surface of a growing crystal either in a specific crystallographic orientation (*i.e.*, orientated attachment), or in a random orientation which requires subsequent structural re-organization for their full integration into the bulk crystal. The latter processes require, however, the initial formation of a larger crystal to which nanoparticles can subsequently attach. This crystal can form from

nanoparticles of different orientations through a process called Oswald ripening, where a larger crystal grows at the expenses of smaller crystals whose size decreases continuously during the crystallization process (De Yoreo et al. 2015).

The occurrence of *CPA* has been proposed as a significant mechanism for the growth of inorganic materials such as anatase (Penn and Banfield 1999; Schindler and Hochella 2016), rutile (Li et al. 2013)], hematite (Park et al. 1996; Shindo et al. 1994), calcium phosphate (Habraken et al. 2013), magnetite (Baumgartner et al. 2013) and goethite (Yuwono et al. 2010), as well as many biologically-mediated systems (e.g. Killian et al. 2009; Mahamid et al. 2008; Politi et al. 2004). Additionally, in complex energy environments, at lower degrees of supersaturation, the formation of precursor metastable nanoparticles and growth by *CPA* may be both thermodynamically and kinetically advantageous in comparison to monomer-by-monomer growth (De Yoreo et al. 2015).

Despite *CPA* in U-O systems having not yet been specifically documented, the following observations in this study suggest the formation of larger uraninite single crystals in the examined samples of the Matoush deposit *via* Oswald ripening and *CPA*:

(1) The occurrence of a single crystal in the core of uraninite aggregates and of nanoparticles in different orientations in their outer rims (Fig. 5c-d);

(2) Different stages of nanoparticle agglomeration and aggregation: singles, clusters and larger aggregates (Figs. 4, 6 and 7).

(3) The occurrence of individual nanoparticles or nano-domains in larger aggregates (Figs. 4, 6 and 7).

IMPLICATIONS

An increasing number of detailed examinations of nano-scale textures associated with mineralization processes in alteration halos of uranium ore deposits indicate the presence of uraninite nanoparticles (Min et al. 2005; Fuchs et al. 2015; Riegler et al. 2016; this study).

These findings suggest that mineralization of uraninite, especially at greater distances to a redox-front, is partially controlled by the formation of these particles. The formation of uraninite nanoparticles can either occur *in situ* or at greater distances from the redox front, but in both cases formation is controlled by the degree of supersaturation and the number of surface sites during heterogeneous nucleation. This study provides evidence for the agglomeration, aggregation and Oswald ripening of uraninite nanoparticles prior, during and after the *CPA* process which resulted subsequently in the formation of larger uraninite crystals. Further examinations of other types of uranium ore deposits at the nanoscale must show whether transport or *in situ* formation of uraninite nanoparticles is predominant at greater distance to redox fronts and whether the formation of more massive uraninite ore bodies is actually a result of *CPA*.

The limited extension of the disseminated mineralization in the alteration halo of the Matoush dyke (on the meter scale) suggests a low mobility of uraninite nanoparticles in the alteration zone of the Matoush ore deposit; most likely due to the high reactivity of the nanoparticles (e.g. Cerrato et al. 2013) and amount of colloidal material in fluids of high ionic strength. In a similar way, potential fluids in a nuclear waste repository containing spent nuclear fuel (which is dominantly UO_2) will be characterized by high ionic strength due to expected low water-rock ratios in a multi-barrier repository system (e.g. Lichtner and Eikenberg 1994, Savage et al. 2000). A high ionic strength would promote the agglomeration of released uraninite nanoparticles and thus facilitate a slowdown of their migration through the multi-barrier system. In contrast, hyperalkaline fluids formed through the interaction of water with concrete and metallic canisters in a repository will have a much higher pH than the pH_{pzc} for uraninite (Lichtner and Eikenberg 1994; Savage et al. 2000; Smith et al. 2015), and would thus result in large repulsive electrostatic double layer forces between colliding uraninite nanoparticles. Experimental studies on agglomeration mechanisms of uraninite nanoparticles at high pH

values and high ionic strength will be thus of great importance for our understanding of the potential transport of nanoparticles in a spent nuclear waste repository.

Acknowledgement

The authors would like to thank two anonymous reviewers for their comments and Associate Editors Julien Mercadier and Keith Putirka for handling the paper. The authors are also grateful to Jon Lafontaine, the geologist from Strateco Resources Inc. who provided access to the Matoush deposit, Paul Alexandre who provided additional data on the samples and deposit, and Tatyana Orlova (University of Notre Dame) for assistance in preparing the sample sections on the FEI Helios Dual Beam 600 NanoLab Focused Ion Beam. This work was supported by NSERC Discovery grants to MS and KK, an NSERC-PDF to AJL and by DE-FG02-07ER15880 US Department of Energy, Basic Energy Science, Heavy Elements Program. MS also acknowledges the Virginia Tech National Center for Earth and Environmental Infrastructure funded under NSF grant 1542100.

REFERENCES CITED

Alessi, D.S., Uster, B., Veeramani, H., Suvorova, E.I., Lezama-Pacheco, J.S., Stubbs, J.E., Bargar, J.R., and Bernier-Latmani, R. (2012) Quantitative separation of monomeric U(IV) from UO_2 in products of U(VI) reduction. Environmental Science and Technology, 46, 6150-6157.

Alexandre, P., Kyser, K., Layton-Matthews, D., Beyer, S., Hiatt, E., and Lafontaine, J. (2015) Formation of the enigmatic Matoush uranium deposit in the Paleoprotozoic Otish Basin, Quebec, Canada. Mineralium Deposita, 50, 825-845.

Bargar, J.R., Bernier-Latmani, R., Giammar, D.E., and Tebo, B.M. (2008) Biogenic Uraninite Nanoparticles and Their Importance for Uranium Remediation. Elements, 4, 407–412.

517 Baumgartner, J., Dey, A., Bomans, P.H.H., Le Coadou, C., Fratzl, P., Sommerdijk, N., and
518 Faivre, D. (2013) Nucleation and growth of magnetite from solution. Nature Materials,
519 12, 310-314.
520 Beyer, S., and Kyser, K. (2015) Mineral paragenesis and U-Pb and Pb-Pb geochronology of
521 sample MT0610-DDH10-303.5m, Matoush zone, Otish Mountains, Quebec. Report to
522 Strateco Resources Inc., p. 1-13.
523 Bots, P., Morris, K., Hibberd, R., Law, G.T., Mosselmans, J.F., Brown, A.P., Doutch, J.,Smith,
524 A.J., and Shaw, S. (2014) Formation of stable uranium(VI) colloidal nanoparticles in
525 conditions relevant to radioactive waste disposal. Langmuir, 30, 14396-14405.
526 Cai, L., Tong, M., Wang, X., and Kim, H. (2014) Influence of clay particles on the transport and
527 retention of titanium dioxide nanoparticles in quartz sand. Environmental Science
528 Technology, 48, 7323-7332.
529 Cerrato, J.M., Ashner, M.N., Alessi, D.S., Lezama-Pacheco, J.S., Bernier-Latmani, R. Bargar,
530 J.R., and Giammar, D.E. (2013) Relative Reactivity of Biogenic and Chemogenic
531 Uraninite and Biogenic Non Crystalline U(IV). Environmental Science Technology, 47,
532 9756-9763.
533 Choi, C.H., Su, Y.W., and Chang, C.H. (2013) Effects of fluid flow on the growth and assembly
534 of ZnO nanocrystals in a continuous flow microreactor. CrystEngComm, 15, 3326-3333.
535 Cölfen, H., and Antonietti, M. (2008) Mesocrystals and Nonclassical Crystallization. 276 p. John
536 Wiley & Sons., West Sussex, England.
537 Derjaguin, B.V., and Landau. L. (1941) Theory of the stability of strongly charged lyophobic sols
538 and of the adhesion of strongly charged particles in solutions of electrolytes. Acta
539 Physico Chimica URSS, 14, 633–662.
540 De Yoreo, J.J., Gilbert, P., Sommerdijk, N., Penn, R.L., Whitelam, S., Joester, D., Zhang, H.Z.,
541 Rimer, J.D., Navrotsky, A., Banfield, J.F., Wallace, A.F., Michel, F.M., Meldrum, F.C.,

Colfen, H., and Dove, P.M. (2015) Crystallization by particle attachment in synthetic, biogenic, and geologic environments. Science, 349, 6247.

Dreissig, I.,Weiss, S.,Hennig, C.,Bernhard, G., and Zanker, H. (2011) Formation of uranium(IV)-silica colloids at near-neutral pH. Geochimica Cosmochimica Acta, 75, 352–367.

Fayek, M., Utsunomiya, S., Ewing, R. C., Riciputi, L. R., and Jensen, K. A. (2003) Oxygen isotopic composition of nano-scale uraninite at the Oklo-Okélobondo natural fission reactors, Gabon. American Mineralogist, 88, 1583–1590.

Fuchs, S., Schumann, D., Williams-Jones, A., and Vali, H. (2015) The growth and concentration of uranium and titanium minerals in hydrocarbons of the Carbon Leader Reef, Witwatersrand Supergroup, South Africa. Chemical Geology, 393, 55–66.

Gatzweiler, R. (1987) Uranium mineralization in the Proterozoic Otish Basin, central Quebec, Canada. In: G. Friedrich, R. Gatzweiler and J. Vogt (Editors), Monograph Series on Mineral Deposits Number 27 - Uranium Mineralization - New Aspects on Geology, Mineralogy, Geochemistry and Exploration Methods, Gebrüder Borntraeger, Berlin-Stuttgart, pp. 27-48.

Goldhaber, M.B., Reynolds, R.L., and Rye, R.O. (1978): Origin of a South Texas roll-type uranium deposit: 11. Sulfide petrology and sulfur isotope studies. Economic Geology, 73, 1690-1705.

Granger, H.C.. and Warren, C.G. (1969): Unstable sulfur compounds and the origin of roll-type uranium deposits. Economic Geology, 64, 160-171.

Habraken, W., Tao, J.H., Brylka, L.J., Friedrich, H., Bertinetti, L., Schenk, A.S., Verch, A., Dmitrovic, V., Bomans, P.H.H., Frederik, P.M., Laven, J., van der Schoot, P., Aichmayer, B., de With, G., DeYoreo, J.J., and Sommerdijk, N. (2013) Ion-association complexes unite classical and non-classical theories for the biomimetic nucleation of calcium phosphate. Nature Communications, 4. 1507.

Hennig, C., Schmeide, K., Brendler, V., Moll, H., Tsushima, S. and Scheinost, A.C. (2007) EXAFS Investigation of U(VI), U(IV), and Th(IV) Sulfato Complexes in Aqueous Solution. Inorganic Chemistry, 46, 5882-5892.

Hostetler, P.B., and Garrels, R.M. (1962): Transportation and precipitation of uranium and vanadium at low temperatures, with special reference to sandstone type uranium deposits. Economic Geology, 57, 137-167.

Hotze, E.M. Phenrat, T. and Lowry, G.V. (2010) Nanoparticle Aggregation: Challenges to Understanding Transport and Reactivity in the Environment. Journal of Environmental Quality, 39, 1909–1924.

Hochella, Jr., M.F. Lower, S.K., Maurice, P.A., Penn, R.L., Sahai, N., Sparks, D.L. and Twining, B.S. (2008) Nanominerals, Mineral Nanoparticles, and Earth Systems. Science, 319, 1631-1635.

Hofmann, B.A. (1999) Geochemistry of Natural Redox Fronts - A Review. Technical Report 99-05, National Cooperative for the Disposal of Radioactive Waste ISSN 1015-2636, 177pp.

Killian, C.E., Metzler, R.A., Gong, Y.U.T., Olson, I.C., Aizenberg, J., Politi, Y., Wilt, F.H., Scholl, A., Young, A., Doran, A., Kunz, M., Tamura, N., Coppersmith, S.N., and Gilbert, P. (2009) Mechanism of Calcite Co-Orientation in the Sea Urchin Tooth. Journal of the American Chemical Society, 131, 18404-18409.

Kretzschmar, R. and Schäfer, T. (2005) Metal Retention and Transport on Colloidal Particles in the Environment. Elements, 1, 205 -210.

Lee, M. (2010) Transmission electron microscopy (TEM) of earth and planetary materials: a review. Mineralogical Magazine, 74, 1-27.

Li, D.S., Soberanis, F., Fu, J., Hou, W.T., Wu, J.Z., and Kisailus, D. (2013) Growth Mechanism of Highly Branched Titanium Dioxide Nanowires via Oriented Attachment. Crystal Growth & Design, 13, 422-428.

592 Lichtner, P.C., and Eikenberg, J. (1994) Propagation of a Hyperalkaline Plume into the
593 Geological Barrier Surrounding a Radioactive Waste Repository. National Cooperative
594 for the Disposal of Radioactive Waste Technical Report, 93-16, 57pp
595 Liyanage, D.D., Rajika J. K. A. Thamali, R.J.K.A., Kumbalatara, A. A. K., Weliwita J. A., and
596 Witharana, S. (2016) An Analysis of Nanoparticle Settling Times in Liquids Journal of
597 Nanomaterials Article ID 7061838, 7 pages, http://dx.doi.org/10.1155/2016/7061838.
598 Long, J.C.S., and Ewing, R.C. (2004) Yucca Mountain: Earth-Science Issues at a Geologic
599 Repository for High-Level Nuclear Waste. Annual Review of Earth and Planetary
600 Sciences, 32, 363-401.
601 Mahamid, J., Sharir, A., Addadi, L., and Weiner, S. (2008) Amorphous calcium phosphate is a
602 major component of the forming fin bones of zebrafish: Indications for an amorphous
603 precursor phase. Proceedings of the National Academy of Sciences of the United States
604 of America, 105, 12748-12753.
605 Min, M., Chen, J., Wang, J., Wei, G. and Fayek, M. (2005) Mineral paragenesis and textures
606 associated with sandstone-hosted roll-front uranium deposits, NW China. Ore Geology
607 Reviews, 26, 51–69.
608 Colfen, H., and De Yoreo, J.J. (2014) Investigating Processes of Nanocrystal Formation and
609 Transformation via Liquid Cell TEM. Microscopy and Microanalysis, 20, 425-436.
610 Olsson, M., Jakobsson, A. M. and Albinsson, Y. (2002) Surface charge densities of two
611 actinide(IV) oxides: UO_2 and ThO_2. Journal of Colloid Interface Sciences, 256, 256–261.
612 Park, G.S., Shindo, D., Waseda, Y., and Sugimoto, T. (1996) Internal structure analysis of
613 monodispersed pseudocubic hematite particles by electron microscopy. Journal of
614 Colloid and Interface Science, 177, 198-207.
615 Pearcy, E.C., Prikryl, J.D., Murphy,W.M. and Leslie, B.W. (1994) Alteration of uraninite from the
616 Nopal I deposit, Pena Blanca District, Chihuahua, Mexico, compared to degradation of

617 spent nuclear fuel in the proposed U.S. high-level nuclear waste repository at Yucca
618 Mountain, Nevada. Applied Geochemistry, 9, 713-73.
619 Penn, R.L., and Banfield, J.F. (1999) Morphology development and crystal growth in
620 nanocrystalline aggregates under hydrothermal conditions: Insights from titania.
621 Geochimica Et Cosmochimica Acta, 63, 1549-1557.
622 Politi, Y., Arad, T., Klein, E., Weiner, S., and Addadi, L. (2004) Sea urchin spine calcite forms
623 via a transient amorphous calcium carbonate phase. Science, 306, 1161-1164.
624 Reynolds, R.L., Goldhaber, M.B., and Carpenter, D.J. (1982): Biogenic and nonbiogenic ore-
625 forming processes in the South Texas uranium district: Evidence from the Panna Maria
626 deposit. Economic Geology, 77, 541-556.
627 Reynolds, R.L., and Goldhaber, M.B. (1978): Origin of a South Texas roll-type uranium deposit:
628 I. Alteration of iron-titanium oxide minerals. Economic Geology, 73, 1677-1689.
629 Reynolds, R.L., and Goldhaber, M.B. (1983): Iron disulfide minerals and the genesis of roll-type
630 uranium deposits. Economic Geology, 78, 105-120.
631 Riegler, T., Beaufort, M.F., Allard, T., Pierson-Wickmann, A.C., and Beaufort, D. (2015)
632 Nanoscale relationships between uranium and carbonaceous material in alteration halos
633 around unconformity-related uranium deposits of the Kiggavik camp, Paleoproterozoic
634 Thelon Basin, Nunavut, Canada, Ore Geology Reviews, 79, 382–391.
635 Savage, D., Stenhouse, M., and Benbow, S. (2000) Evolution of Near-Field Physico-Chemical
636 Characteristics of the SFR Repository. Swedish Nuclear Power Inspectorate (SKI).
637 Report, 00:49 Project Number 99136, 109pp.
638 Schindler, M., Fayek, M., and Hawthorne, F.C. (2010) Uranium-rich opal from the Nopal I
639 uranium deposit, Peña Blanca, Mexico: evidence for the uptake and retardation of
640 radionuclides. Geochimica et Cosmochimica Acta, 74, 187–202.

Schindler, M., and Hochella, M.F. (2015) Nanomineralogy is a new dimension in understanding illusive geochemical processes in soils: The case of low solubility index elements. Geology.44, 515-519.

Schmidt, M., Lee, S.S., Wilson, R.E., Knope, K.E., Bellucci, F., Eng, P.J., Stubbs, J.E., Soderholm, L., and Fenter, P. (2013) Surface-Mediated Formation of Pu(IV) Nanoparticles at the Muscovite-Electrolyte Interface. Environmental Science & Technology, 47, 14178-14184.

Schmidt, M., Wilson, R.E., Lee, S.S., Soderholm, L., and Fenter, P. (2012) Adsorption of Plutonium Oxide Nanoparticles. Langmuir, 28, 2620-2627.

Shindo, D., Park, G.S., Waseda, Y., and Sugimoto, T. (1994) Internal structure-analysis of monodispersed ppeanut-type hematite particles produced by the gel-sol method. Journal of Colloid and Interface Science, 168, 478-484.

Singer, D.M., Farges, F., and Brown, G.E. Jr. (2009) Biogenic nanoparticulate UO_2: Synthesis, characterization, and factors affecting surface reactivity. Geochimica et Cosmochimica Acta, 73, 3593–3611.

Smith, K.F., Bryan, N.D. Swinburne, A.D., Bots, P. Shaw, S., Natrajan, L.S., Frederick, J., Mosselmans, W., Livens, F.R., and Morris, K. (2015) U(VI) behaviour in hyperalkaline calcite systems. Geochimica et Cosmochimica Acta, 148, 343–359.

Suzuki, Y., Mukai, H., Ishimura, T., Yokoyama, T.D., Sakata, S. Hirata, T., Iwatsuki, T. and Mizuno, T. (2015) Formation and Geological Sequestration of Uranium Nanoparticles in Deep Granitic Aquifer. Scientific Reports, 6:22701, DOI: 10.1038/srep22701.

Suzuki, Y., Kelly, S. D., Kemner, K. M., and Banfield, J. F. (2002) Radionuclide contamination: Nanometre-size products of uranium bioreduction. Nature, 419, 134.

Verwey, E., Overbeek, J., and van Nes, K. (1948) The theory of the stability of liophobic colloids: The interaction of sol particles having an electric double layer. Elsevier, Amsterdam.

667 Vilks, P., Cramer, J.J., Bachinski, D.B. Doern,D.C., and Miller, H.G. (1993) Studies of colloids
668 and suspended particles, Cigar Lake uranium deposit, Saskatchewan, Canada. Applied
669 Geochemistry, 8, 605-616.
670 Wang, Y., Frutschi, M., Suvorova, E., Phrommavanh, V., Descostes., Osman, A.A.A., Geipel,
671 G., and Bernier-Latmani, R. (2013) Mobile uranium (IV)-bearing colloids in a mining-
672 impacted wetland. Nature Communications, 4, 2942-2951.
673 Weber, F.A., Voegelin, A., Kaegi, R. and Kretzschmar, R. (2009) Contaminant mobilization by
674 metallic copper and metal sulphide colloids in flooded soil. Nature Geoscience, 2, 267-
675 271.
676 Wirth, R. (2009) Focused ion beam combined with SEM and TEM: Advanced analytical tools for
677 studies of chemical composition, microstructure and crystal structure in geomaterials on
678 a nanometer scale. Chemical Geology, 261, 217–229.
679 Yuwono, V.M., Burrows, N.D., Soltis, J.A., and Penn, R.L. (2010) Oriented Aggregation:
680 Formation and Transformation of Mesocrystal Intermediates Revealed. Journal of the
681 American Chemical Society, 132, 2163-8.
682

683 **Figure Captions**

684 **Figure 1.** Location of the Matoush deposit in the Otish Basin, Central Quebec, Canada,
685 schematic cross section of the Matoush dyke complex (modified from Alexandre et al.
686 2015) and proposed flow directions of the U^{6+} solutions (indicated with arrows).
687

688 **Figure 2.** Optical micrograph image, μ-XRF and SEM-EDS chemical distribution maps of the
689 sample from the outer alteration zone of the Matoush ore deposit; areas depicted in the
690 chemical distribution maps are indicated with rectangles and arrows in the optical image
691 as well as in the *μ*-XRF and SEM-BSE maps and images, respectively; (a) μ-XRF image
692 depicting the total counts of X-rays recorded during mapping of the chemical distribution

693 of all selected elements; (b)-(e) μ-XRF chemical distribution maps of the area depicted in
694 (a); elements and associated colours are given below each map; (f) optical micrograph
695 image; (g) SEM-EDS chemical maps for U in white, Si in red and P in green; the location
696 of the extraction of FIB Section 1 is indicated with a yellow rectangle; (h) SEM-BSE
697 image of finely distributed uraninite in eskolaite; the area shown in (i) is indicated with a
698 red-framed rectangle; (i) SEM-BSE image of the interface between uraninite and
699 eskolaite, which is composed primarily of Cr-rich mica; the location of the extraction of
700 Section 2 is shown with a yellow rectangle; areas dominantly composed of eskolaite, Cr-
701 dravite, fluorapatite, uraninite and Cr-rich mica are labelled Es, Dr, Ap, Ur and Cc,
702 respectively.
703
704 **Figure 3.** (a) STEM image of Section 1; areas shown in Figures 4, 5a-b and 5d are indicated
705 with white- and black-framed rectangles as labelled; (b) SEM image of Section 2 after
706 extraction and thinning of a selected area; the area shown in (c) is indicated with a white
707 rectangle; (c) STEM image of the thinned area in Section 2 as depicted in (b); a white-
708 framed rectangle indicates the location of the image shown in Figure 6; areas shown in
709 Figures 7a-c and 7d-e are labeled accordingly; areas predominantly composed of
710 eskolaite, fluorapatite, uraninite, Cr-rich mica and galena and an amorphous Cr-rich
711 oxide matrix are labelled Es, Ap, Ur, Cm, Gn and Am respectively.
712
713 **Figure 4.** Images and SAED pattern from Section 1: (a) TEM image of a distorted (111) face of
714 a galena cubooctahedron (111) and surroundings in Section 1 (as depicted in Figure
715 3a); SAED pattern on the right side indicate the presence of a uraninite single crystal (Ur
716 single crystal) and areas composed of nano-domains or nanoparticles of different
717 orientations (Ur NP; see text for details); (b)-(d) interfaces between (b) fluorapatite (Ap)
718 and uraninite (Ur) and (c)-(d) galena (Gn) and uraninite (Ur) (indicated with red lines);

719 nano-domains of uraninite (framed with white dashed lines) can be recognized on the
720 lattice fringes with different orientations (white solid lines); lattice fringes in the surface
721 structures of fluorapatite and galena are also indicated with white solid lines;
722 characteristic *d*-spacings and *(hkl)* indices are given for the respective lattice fringes.
723
724 **Figure 5.** Images, chemical maps and SAED pattern taken from Section 1: (a)-(b) STEM image
725 and STEM-EDS chemical distribution map for U (blue), Si (red) and Fe (green) of the
726 interface between uraninite and Cr-rich mica (as depicted in Figure 3); numbers in (a)
727 indicate the locations from where the SAED pattern in (c) were taken; (c) SAED pattern
728 from a transect across the interface between uraninite and Cr-rich mica; numbers
729 indicate the respective locations depicted in (a); (d) the surface of the uraninite grain
730 depicted in Figure 3a; the locations of three nanoparticles of uraninite are indicated with
731 arrows.
732
733 **Figure 6.** Images and chemical maps from Section 2: (a)-(b) STEM image and STEM-EDS
734 chemical map for U (blue), Si (red) and Fe (green) of the interface between uraninite and
735 the Cr-rich oxide matrix in Section 2 (as depicted in Figure 4c); (c) STEM-EDS chemical
736 distribution map for U (blue), Si (red) and Fe (green) of a single nanoparticle of uraninite;
737 (d) STEM image of an amorphous Cr-rich oxide matrix surrounded by individual and
738 aggregated uraninite nanoparticles, the corresponding EDS-STEM distribution map for
739 Si (red) Cr (green), and U (blue) is shown in the lower left corner; the area shown in (e)
740 is indicated with white circles in the STEM and EDS-STEM image; (e) TEM image of
741 needles of bracewellite ($Cr^{3+}OOH$) in an amorphous Cr-rich oxide matrix; (f) high
742 resolution TEM image of bracewellite single crystals with visible lattice fringes
743 (highlighted with solid white lines).
744

745 **Figure 7.** Images and chemical maps from Section 2: (a) STEM image of individual and
746 agglomerated and aggregated nanocrystals of uraninite along the Cr-rich mica surface in
747 Section 2; the occurrence of small inclusions of bracewellite are indicated with white
748 arrows; (b) TEM image of single and clustered uraninite nanoparticles; (c) individual
749 nanoparticle of coffinite depicting an ellipsoid shape; (d)-(e) STEM image and STEM-
750 EDS chemical distribution map for U (blue) and Cr (orange) of uraninite nanoparticles
751 clustered around inclusions of bracewellite (indicated with arrows)
752
753 **Figure 8.** Flow chart showing a conceptual model for the occurrence of at least two late
754 stage fluid events in the outer rims of the Matoush basin
755
756
757
758
759
760
761
762

This is a preprint, the final version is subject to change, of the American Mineralogist (MSA)
Cite as Authors (Year) Title. American Mineralogist, in press.
(DOI will not work until issue is live.) DOI: http://dx.doi.org/10.2138/am-2017-5984

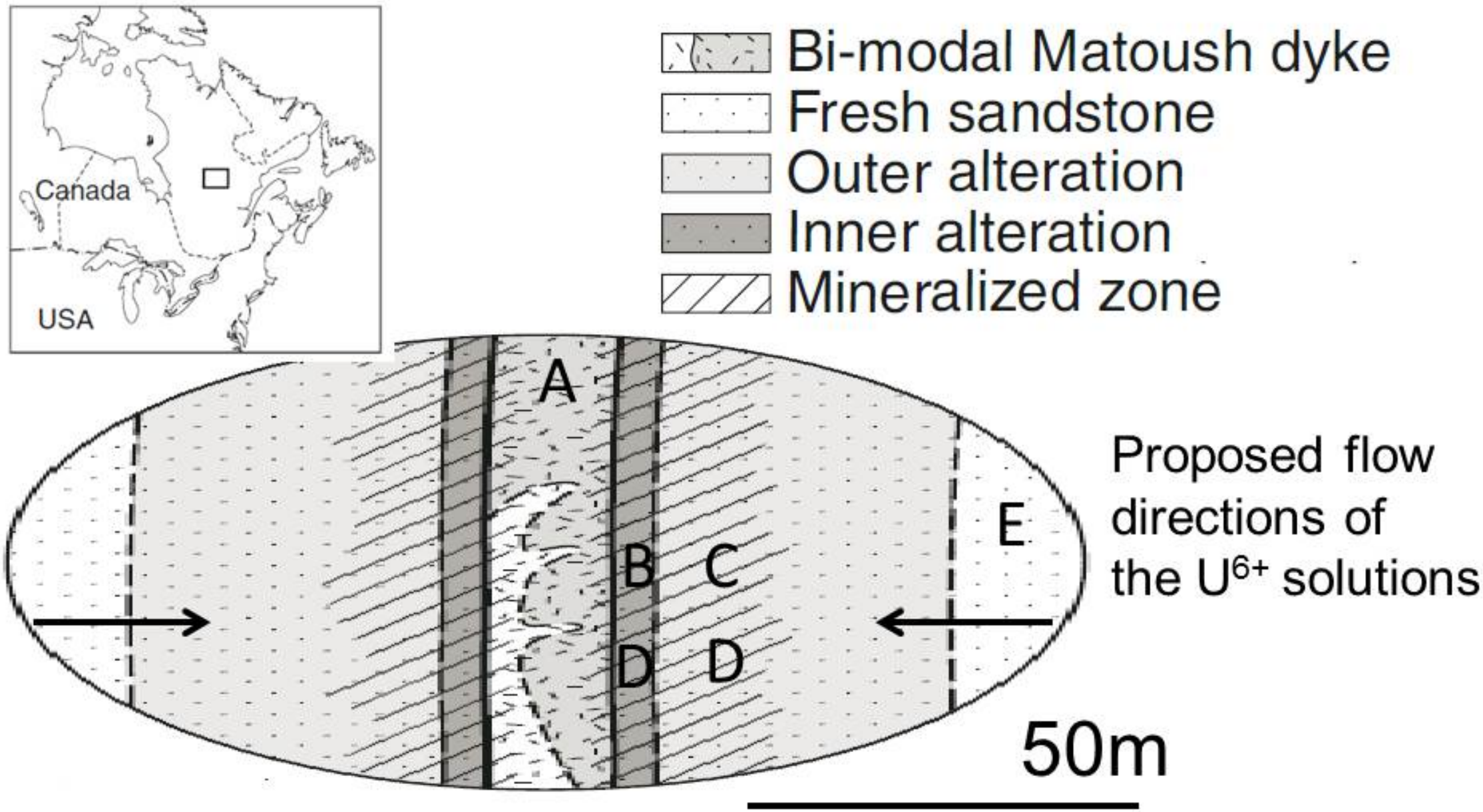

Fig. 1

This is a preprint, the final version is subject to change, of the American Mineralogist (MSA)
Cite as Authors (Year) Title. American Mineralogist, in press.
(DOI will not work until issue is live.) DOI: http://dx.doi.org/10.2138/am-2017-5984

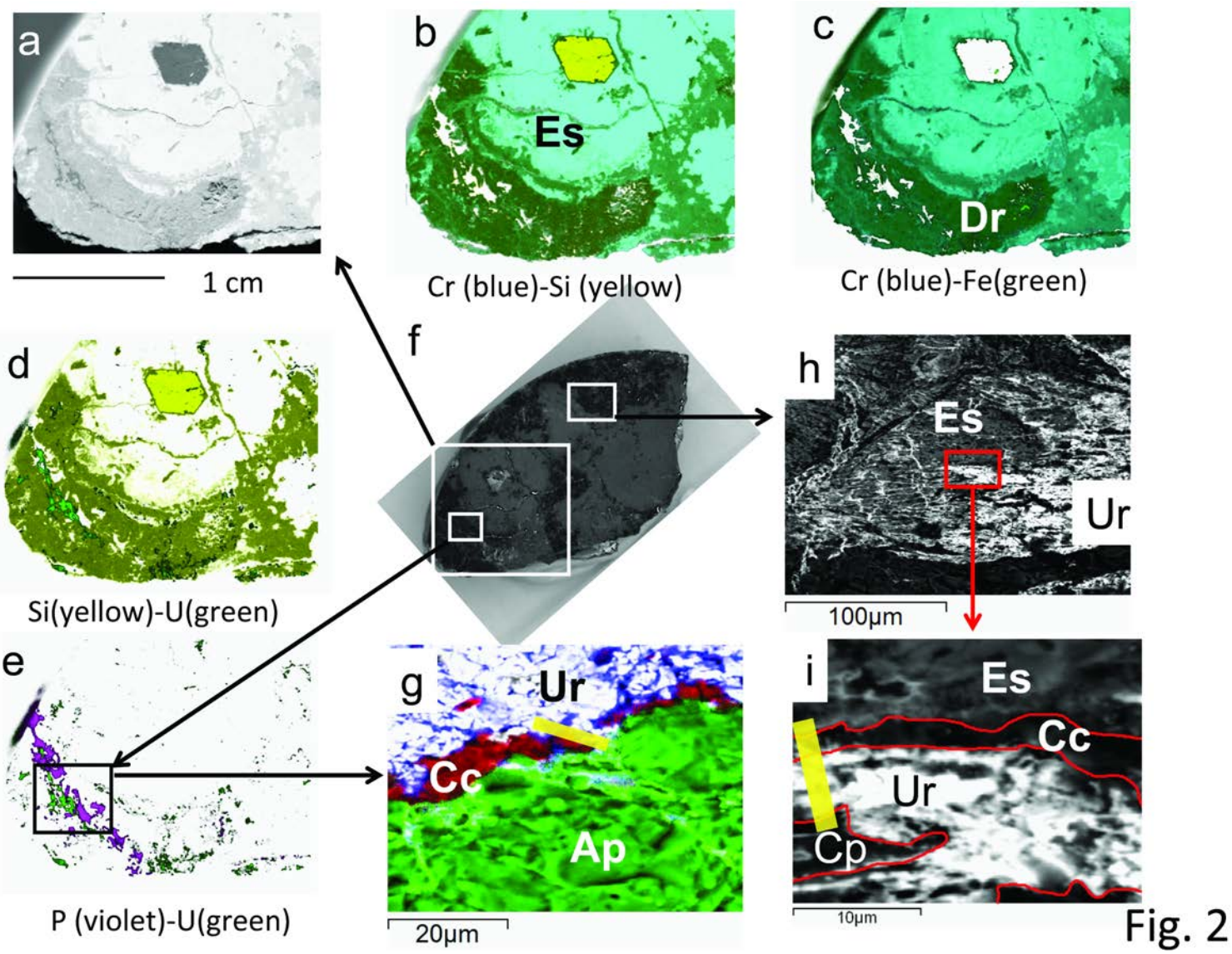

Fig. 2

This is a preprint, the final version is subject to change, of the American Mineralogist (MSA)
Cite as Authors (Year) Title. American Mineralogist, in press.
(DOI will not work until issue is live.) DOI: http://dx.doi.org/10.2138/am-2017-5984

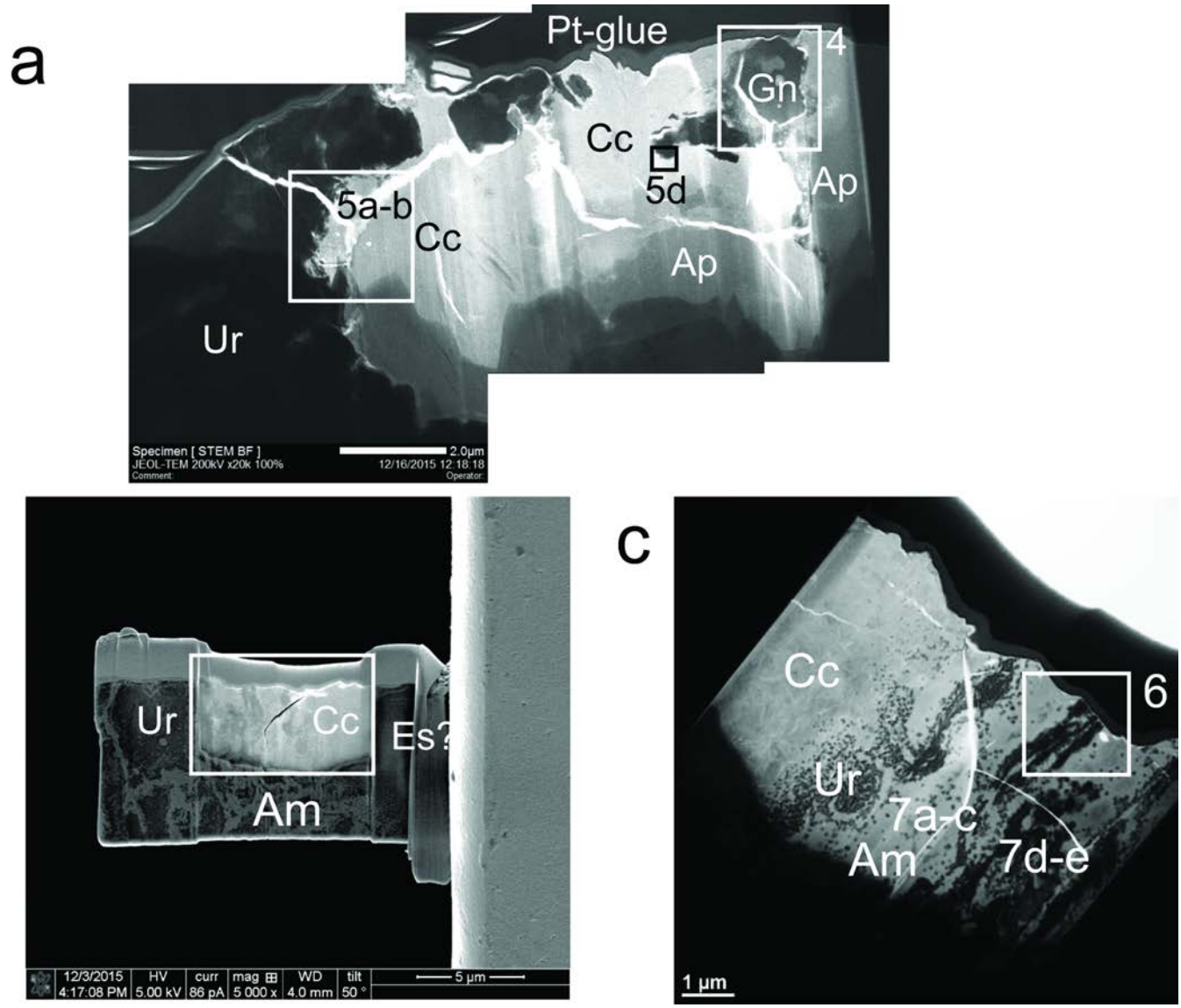

Fig. 3

This is a preprint, the final version is subject to change, of the American Mineralogist (MSA)
Cite as Authors (Year) Title. American Mineralogist, in press.
(DOI will not work until issue is live.) DOI: http://dx.doi.org/10.2138/am-2017-5984

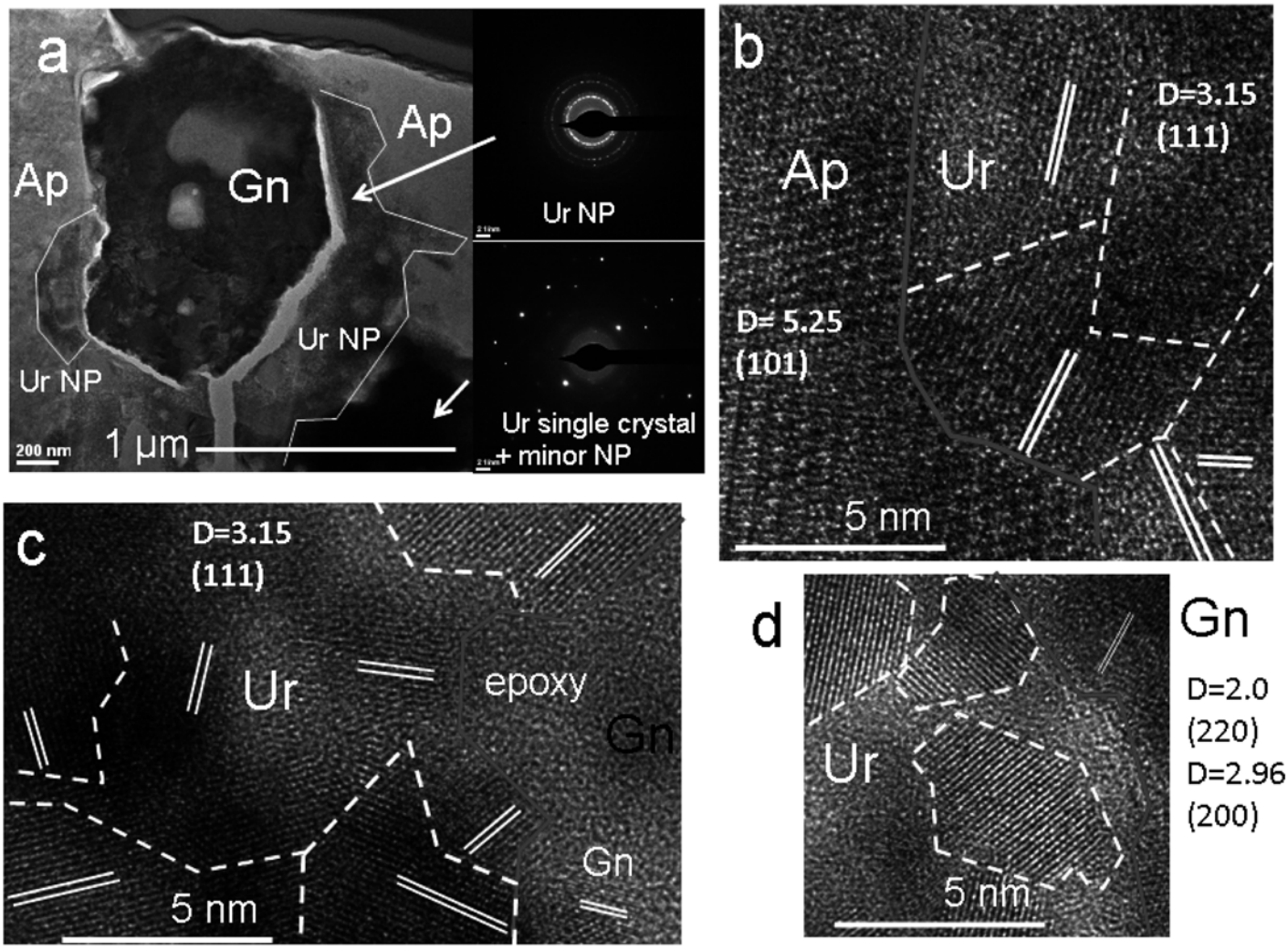

Fig. 4

This is a preprint, the final version is subject to change, of the American Mineralogist (MSA)
Cite as Authors (Year) Title. American Mineralogist, in press.
(DOI will not work until issue is live.) DOI: http://dx.doi.org/10.2138/am-2017-5984

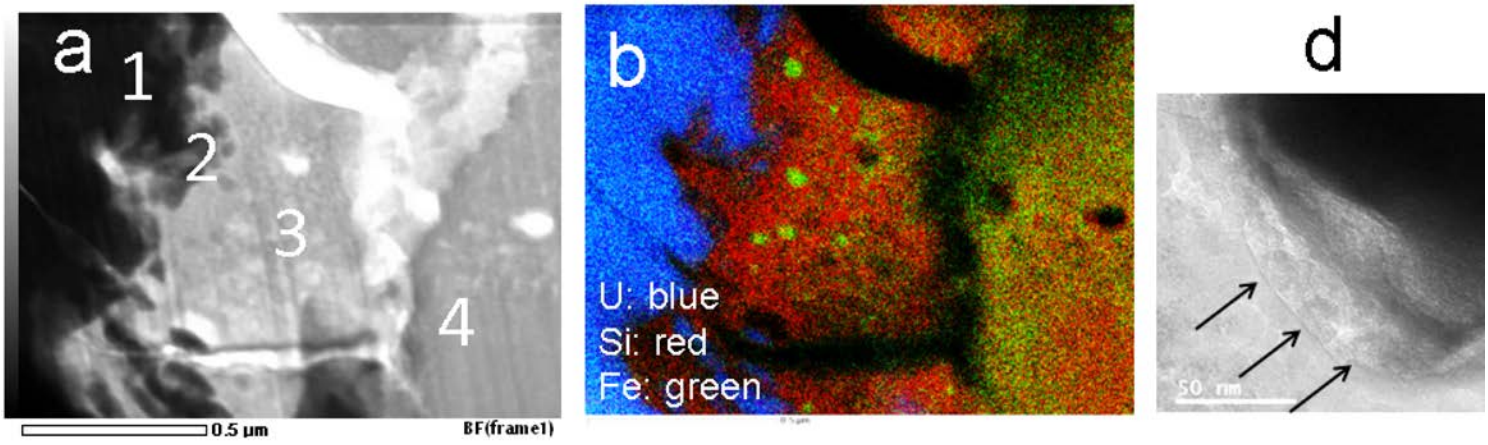

Fig. 5

This is a preprint, the final version is subject to change, of the American Mineralogist (MSA)
Cite as Authors (Year) Title. American Mineralogist, in press.
(DOI will not work until issue is live.) DOI: http://dx.doi.org/10.2138/am-2017-5984

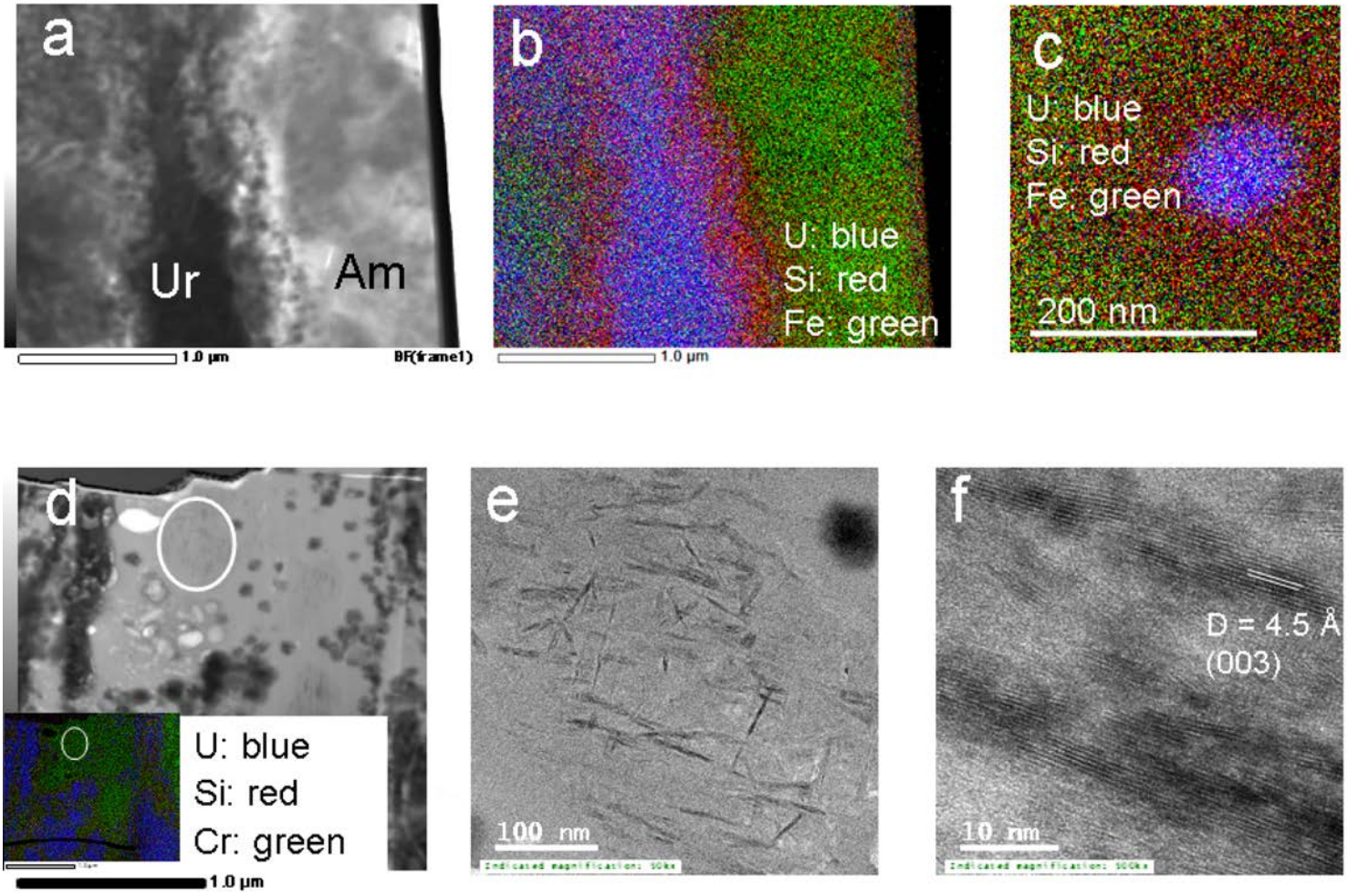

Fig. 6

This is a preprint, the final version is subject to change, of the American Mineralogist (MSA)
Cite as Authors (Year) Title. American Mineralogist, in press.
(DOI will not work until issue is live.) DOI: http://dx.doi.org/10.2138/am-2017-5984

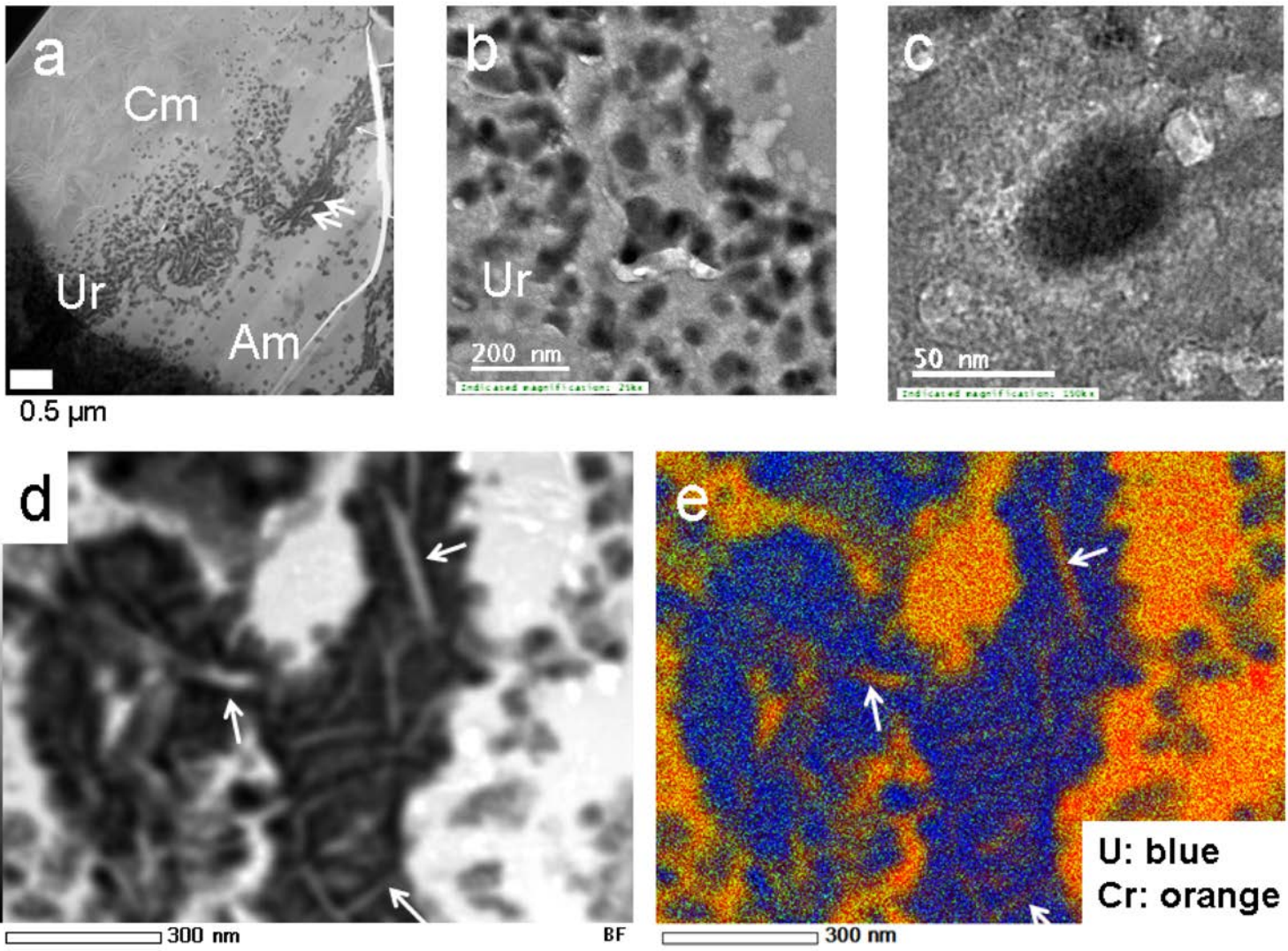

Fig. 7

This is a preprint, the final version is subject to change, of the American Mineralogist (MSA)
Cite as Authors (Year) Title. American Mineralogist, in press.
(DOI will not work until issue is live.) DOI: http://dx.doi.org/10.2138/am-2017-5984

Late-stage fluid events in the Matoush deposit after the main uranium mineralization event